Batteries & Supercaps

Research Article
doi.org/10.1002/batt.202400652

Chemistry
Europe
European Chemical
Societies Publishing

www.batteries-supercaps.org

Enhanced Electrochemical Performance of Li-rich Cathode Materials by Al Doping

Busra Cetin,[a] Tugce Gul Idinak,[a] and Neslihan Yuca*[a, b]

Li-rich oxides are the most promising of the high-voltage cathode materials with their high specific capacity. However, Li-rich cathode materials suffer from structural instability, voltage degradation, and capacity fading upon cycling. Al-doping can improve electrochemical performance by stabilizing the structure and suppressing the phase transitions for Li-rich cathodes. In this paper, we investigate the effect of different amounts of Al with the general formula $Li_{1.2}Mn_{0.54-x}Ni_{0.13}Co_{0.13}Al_xO_2$ and $Li_{1.2-x}Mn_{0.54}Ni_{0.13}Co_{0.13}Al_xO_2$ (x = 0.02, 0.05, 0.1) cathode materials. The Li and Mn elements were replaced by Al, and the electrochemical performance was compared to pristine $Li_{1.2}Mn_{0.54}Ni_{0.13}Co_{0.13}O_2$. The Li and Mn elements were replaced by Al, and the electrochemical performance was compared. The impact of substitution of Mn and Li by Al on the structural and morphological properties has been investigated by scanning electron microscopy (SEM) and X-ray diffraction (XRD). The charge and discharge tests show that doping with Al substitution leads to improved electrochemical performance, enhancing both the cycling stability and rate capability of the Li-rich cathode materials. Along with the improved specific capacities, these materials demonstrate superior rate performance, particularly for the composition with the lowest Al content.

Introduction

Li-ion batteries (LIBs) have built a global revolution for modern society over the past 20 years with their potential to provide sustainable and distributed energy supply. The LIB sector has become the dominant power source for computers, mobile phones, cameras, electric cars, and large-scale industrial energy storage solutions due to its rapid development. Although significant advancements have been made in the utilization of LIBs, there is still potential for further enhancements.[1–5] Li- and Mn-rich oxides (LMRO), first introduced by Thackeray et al. in 1991,[6] have attracted significant interest due to their exceptionally high specific capacities exceeding 250 mAhg⁻¹ and elevated operating voltages, making them promising candidates for next-generation LIBs.[7,8] However, LRMOs suffer notable difficulties, including structural instability, voltage degradation, and limited capacity to maintain high cycle rates over longer cycles. These problems are primarily caused by the irreversible release of oxygen, the migration of transition metal (TM) ions, and phase transitions from layered structures to spinel or rock-salt.[9–11] The substitution of transition metal (TM) ions with dopant elements, such as Al, Mg, and Cr, is a widely used method to facilitate crystalline phase changes induced by the migration of transition metal ions at high charge voltages. Typically, the oxidation states of transition metals (Ni, Mn, and Co) in LMRO cathodes are +2, +4, and +3, respectively. The oxidation states of Ni, Mn, and Co may vary when the oxidation state of the doped ions differs from that of the transition metal. Replacing transition metal ions with other metal ions can be beneficial for enhancing several properties, such as material stability, ion conductivity, diffusion channels, electrical conductivity, and M—O bonding.[12–16]

One effective strategy to mitigate these problems is the doping of LMROs with Al, which has been shown to enhance the electrochemical performance by stabilizing the structure and suppressing detrimental phase transitions.[17,18] Al doping in LRMOs can significantly improve cycle stability and rate performance through multiple mechanisms. Al^{3+} ions substitute for TM ions (Ni, Co, Mn) in the lattice, which helps reduce charge transfer resistance and stabilize the oxygen lattice, thereby reducing irreversible oxygen loss and mitigating phase transitions during cycling.[19,20] Additionally, the formation of stronger Al—O bonds compared to TM—O bonds enhances the structural integrity of the cathode material, particularly at higher temperatures.[21,22] Cai et. al.[23] found that the substitution of Mn in the material has a significant effect on enhancing thermal stability, preventing irreversible oxygen release, and reducing voltage/capacity fading in the LMROs.

Lithium-deficient layered LMRO cathodes can demonstrate remarkable electrochemical properties. Lithium-deficient LMRO cathodes exhibit the existence of lithium vacancies, leading to the development of nickel-rich surfaces and spinel phase coatings. The implementation of the doping approach can

[a] B. Cetin, T. Gul Idinak, N. Yuca
Enwair Energy Technologies Corporation
Huzur Mah. Ahmet Bayman Cad. No:2/4 Sariyer, Istanbul / Turkiye

[b] N. Yuca
Energy Institute
Istanbul Technical University
ITU Ayazaga Campus, Energy Institute Building, 34469, Maslak, Istanbul / Turkiye
E-mail: nyuca@itu.edu.tr

Batteries & Supercaps

Research Article
doi.org/10.1002/batt.202400652

Chemistry
Europe
European Chemical
Societies Publishing

effectively mitigate oxygen loss and improve the structural stability of the cathodes.[24–26] Song et al.[27] investigated the impact of Al substitution on $Li_{1.2}Mn_{0.54}Ni_{0.13}Co_{0.13}O_2$ morphology, structure, and electrochemical properties. Results show significant improvement in material performance, with a current density of 1 C and a capacity retention rate of 92.8% after 100 cycles.

In this study, we investigated the effect of the substitution of Li and Mn with Al. The electrochemical performance of $Li_{1.2}Mn_{0.54-x}Ni_{0.13}Co_{0.13}Al_xO_2$ and $Li_{1.2-x}Mn_{0.54}Ni_{0.13}Co_{0.13}Al_xO_2$ (x = 0.02, 0.05, 0.1) was investigated and compared with pristine cathode. The designation of the LMRO cathodes is given in Table 1.

Experimental

The pristine cathode with formula of the $Li_{1.2}Mn_{0.54}Ni_{0.13}Co_{0.13}O_2$, $Li_{1.2}Mn_{0.54-x}Ni_{0.13}Co_{0.13}Al_xO_2$ (x = 0.02, 0.05, 0.1), and $Li_{1.2-x}Mn_{0.54}Ni_{0.13}Co_{0.13}Al_xO_2$ (x = 0.02, 0.05, 0.1) cathode materials were synthesized using the citric-acid assisted sol-gel method. The designation of the samples and targeted compositions is given in Table 1.

A stoichiometric amount of $LiCH_3COO \cdot 2H_2O$ (lithium acetate dihydrate, Sigma-Aldrich), $Mn(CH_3COO)_2 \cdot 4H_2O$ (manganese (II) acetate tetrahydrate, Sigma-Aldrich), $Ni(CH_3COO)_2 \cdot 4H_2O$ (Nickel (II) acetate tetrahydrate, Sigma-Aldrich), $Co(NO_3)_2 \cdot 4H_2O$ (Cobalt (II) acetate tetrahydrate, Sigma-Aldrich), $Al(NO_3)_3 \cdot 9H_2O$ (aluminum nitrate nonahydrate, Sigma-Aldrich) was dissolved in de-ionized water. Excess Li (5%) was added to compensate for the Li loss at the high temperature calcination process. The citric acid solution was added dropwise to the mixed solution. The chelating agent/metal ions molar ratio was optimized to be 2:1. The pH of the

mixed solution was adjusted to 9 by using ammonium hydroxide. Then, the mixed solution was heated at 80 °C under stirring until a gel was obtained. The gel was placed in a vacuum drying box at 120 °C for 12 h to form a dry gel. The dry gel was calcinated at 500 °C for 5 h and at 900 °C for 10 h in an air atmosphere. The pristine LMR cathode was prepared in the same way without adding $Al(NO_3)_3 \cdot 9H_2O$ as a reference material for investigating the effect of Al dopant on Li-rich cathodes.

LMRO cathodes were characterized by Inductively Coupled Plasma Mass Spectroscopy (ICP-MS, Agilent 7700x), X-ray diffraction (XRD, Rigaku MiniFlex 600, Cu Kα radiation, λ = 0.15406 nm), scanning electron microscopy (SEM, Hitachi SU5000), energy dispersive X-ray spectroscopy (EDS, Oxford XMax-40), and electrochemical impedance spectroscopy (EIS, Gamry Instrument Interface 1010E) for elemental, phase, and morphological analysis. The valence states of metal-ions were determined by X-ray photoelectron spectroscopy (XPS, Thermo K-alpha). Electrochemical tests were performed with CR2032-type coin cells, fabricated with the cathode electrode, lithium metal reference anode. The formation cycles were conducted at 0.25 C in two charge/discharge cycles in the voltage range of 2.8–4.6 V. Followed by electrochemical activation of the materials, galvanostatic charge/discharge tests were performed five times at 0.1 C, 0.2 C, 1 C, and 2 C, respectively, and finally at 0.1 C. EIS measurements were performed under open circuit voltage (OCV) with frequency range of 1 MHz to 0.1 Hz, and the AC amplitude was 10 mV.

Results and Discussion

The elemental analysis results of the materials are presented in Table 2. The chemical compositions of the samples closely match the target compositions, indicating successful synthesis and minimal deviation from the intended stoichiometry. This

Table 1. Designations of the samples and their targeted compositions.

Sample	Targeted Composition	Dopant Level
LMR	$Li_{1.2}Mn_{0.54}Ni_{0.13}Co_{0.13}O_2$	Pristine Cathode
LMR–Al1	$Li_{1.2}Mn_{0.52}Ni_{0.13}Co_{0.13}Al_{0.02}O_2$	0.02 at.% Al on Mn-site
LMR–Al2	$Li_{1.2}Mn_{0.49}Ni_{0.13}Co_{0.13}Al_{0.05}O_2$	0.05 at.% Al on Mn-site
LMR–Al3	$Li_{1.2}Mn_{0.44}Ni_{0.13}Co_{0.13}Al_{0.1}O_2$	0.1 at.% Al on Mn-site
LMR–Al4	$Li_{1.18}Mn_{0.54}Ni_{0.13}Co_{0.13}Al_{0.02}O_2$	0.02 at.% Al on Li-site
LMR–Al5	$Li_{1.15}Mn_{0.54}Ni_{0.13}Co_{0.13}Al_{0.05}O_2$	0.05 at.% Al on Li-site
LMR–Al6	$Li_{1.10}Mn_{0.54}Ni_{0.13}Co_{0.13}Al_{0.1}O_2$	0.1 at.% Al on Li-site

**Table 2.** ICP-MS analysis results of atomic percentage (at. %) for LMRO cathode materials.

Samples	at.% Li		at.% Mn		at.% Co		at.% Ni		at.% Al	
	Theoretical	ICP	Theoretical	ICP	Theoretical	ICP	Theoretical	ICP	Theoretical	ICP
LMR	60.00	59.50	27.00	27.24	6.50	6.72	6.50	6.54	0	0
LMR–Al1	60.00	58.85	26.00	26.73	6.50	6.76	6.50	6.60	1.00	1.05
LMR–Al2	60.00	58.92	24.50	25.06	6.50	6.75	6.50	6.58	2.50	2.69
LMR–Al3	60.00	58.05	22.00	22.94	6.50	6.90	6.50	6.73	5.00	5.38
LMR–Al4	59.00	58.83	27.00	27.02	6.50	6.63	6.50	6.48	1.00	1.03
LMR–Al5	57.50	57.83	27.00	26.73	6.50	6.54	6.50	6.41	2.50	2.50
LMR–Al6	55.00	55.91	27.00	26.32	6.50	6.48	6.50	6.33	5.00	4.96

Batteries & Supercaps

Research Article
doi.org/10.1002/batt.202400652

Chemistry Europe

European Chemical
Societies Publishing

consistency suggests that the preparation process was well-controlled, ensuring that the desired chemical proportions were achieved in the final product. The SEM images with EDS line profiles are given in Figure 1 for Al-doped LMRO cathodes and compared with pristine cathode which is given in Figure S1 (Supporting Information). SEM images of the materials indicate that they consist of primary and secondary particles with a homogeneous distribution, generally ranging in size from 100 to 300 nm. Moreover, the Al dopant has not caused any significant changes in the morphology of the materials. The morphology and size of the particles are almost identical among all samples, and the particle size has not changed significantly with different dopant levels. All samples consist of clear-edged polyhedral nanoparticles. These morphological results were consistent with previous studies.[28–30] The elements Ni, Co, and Mn are uniformly distributed within the particles, as evidenced by the EDS line profiles.

The structure of LRMO cathode materials plays a crucial role in determining their electrochemical reaction mechanisms and overall performance. These materials are generally classified within the $xLi_2MnO_3(1-x)LiMO_2$ composite framework, where M represents transition metals such as Ni, Co, and Mn. This structural model is best described using a two-phase approach, which consists of a monoclinic Li_2MnO_3 (C2/m) phase and a layered $LiMO_2$ (R3m) phase. The presence of the Li_2MnO_3 phase introduces additional oxygen redox activity and contributes to structural stabilization, albeit at the cost of voltage fade during extended cycling. According to this structural model, the interlayer spacing of the (001) plane in the Li_2MnO_3 phase and the (003) plane in the layered $LiTMO_2$ phase is both close to 4.7 Å.[31–36] This close interplanar spacing is essential, as it influences lithium-ion diffusion kinetics and electrochemical performance. Figure 2 presents the Rietveld refinement results

and XRD patterns of the Al-doped LMRO cathode materials, compared with the pristine cathode (Supporting Information Figure S2). It is observed that all major diffraction peaks in the XRD patterns correspond to the layered $LiMO_2$ structure, confirming that Al doping does not introduce secondary phases or impurity phases. The weak peaks in the 20°–23° 2θ region correspond to the superlattice reflections of the monoclinic Li_2MnO_3 phase (C2/m space group). The clear separation of the (006)/(102) peaks around 38° and (108)/(110) peaks around 66° further confirms that all samples exhibit a well-organized layered structure with minimal cation disorder.[28,37,38]

Figure 3 provides a magnified view of the (003) and (104) peaks, showing a progressive shift toward lower 2θ values as the Al doping concentration increases. This shift is particularly pronounced at doping levels of 0.05 and 0.1, indicating an expansion of the interlayer spacing. In XRD analysis, a lower diffraction angle (2θ) corresponds to a larger interlayer spacing, suggesting that Al doping influences the structural framework. In layered cathode materials, an increase in interlayer spacing facilitates lithium diffusion and enhances high-rate capability by reducing the energy barrier for Li^+ migration.[39,40] The calculated lattice parameters, summarized in Table 3, further validate these structural modifications. The lattice parameter 'c' is particularly significant, as it directly corresponds to the distance between interlayers within the structure. An increase in the c parameter indicates greater interlayer spacing, allowing for easier lithium-ion insertion and extraction, which is beneficial for rate capability and cycling performance. Moreover, the c/a ratio reflects cation ordering, where a higher c/a value suggests a more stable hexagonal crystal structure.[42–44] The gradual increase in the c/a ratio in Al-doped materials compared to the pristine cathode suggests that Al is incorporated into the Li and
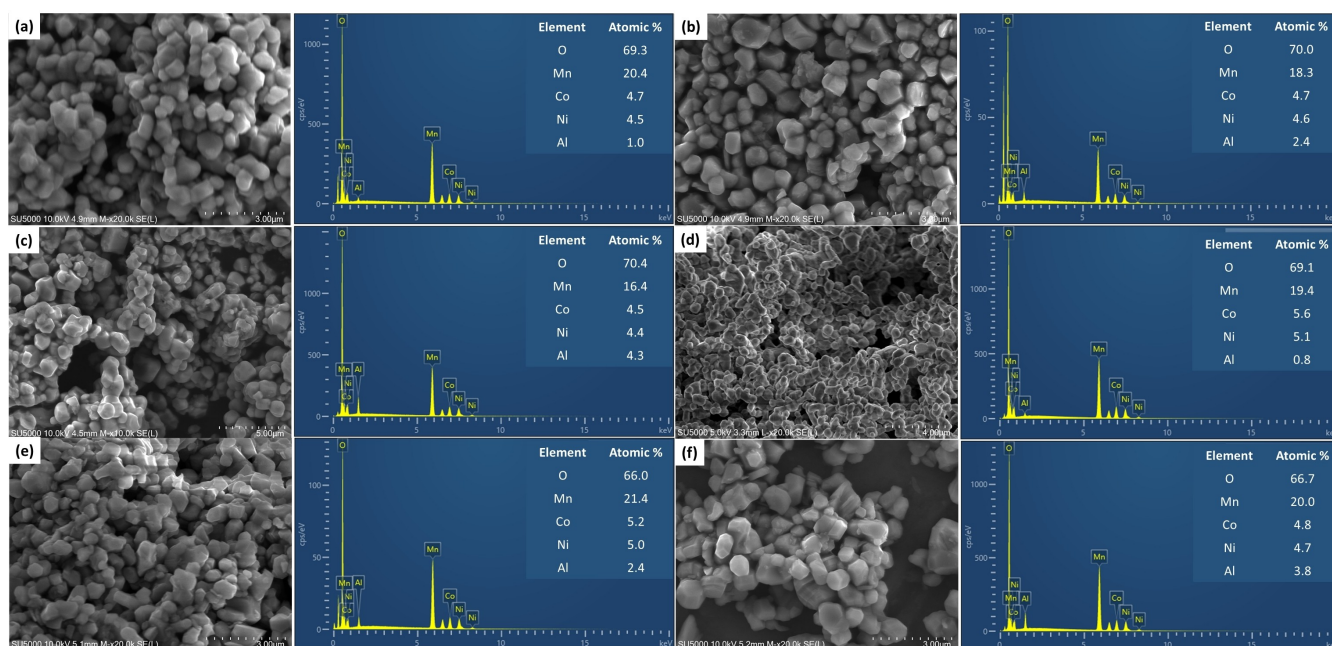
Figure 1. SEM images with EDS spectrums (a) LMR–Al1, (b)LMR–Al2, (c) LMR–Al3, (d) LMR–Al4, (e) LMR–Al5, (f) LMR–Al6.
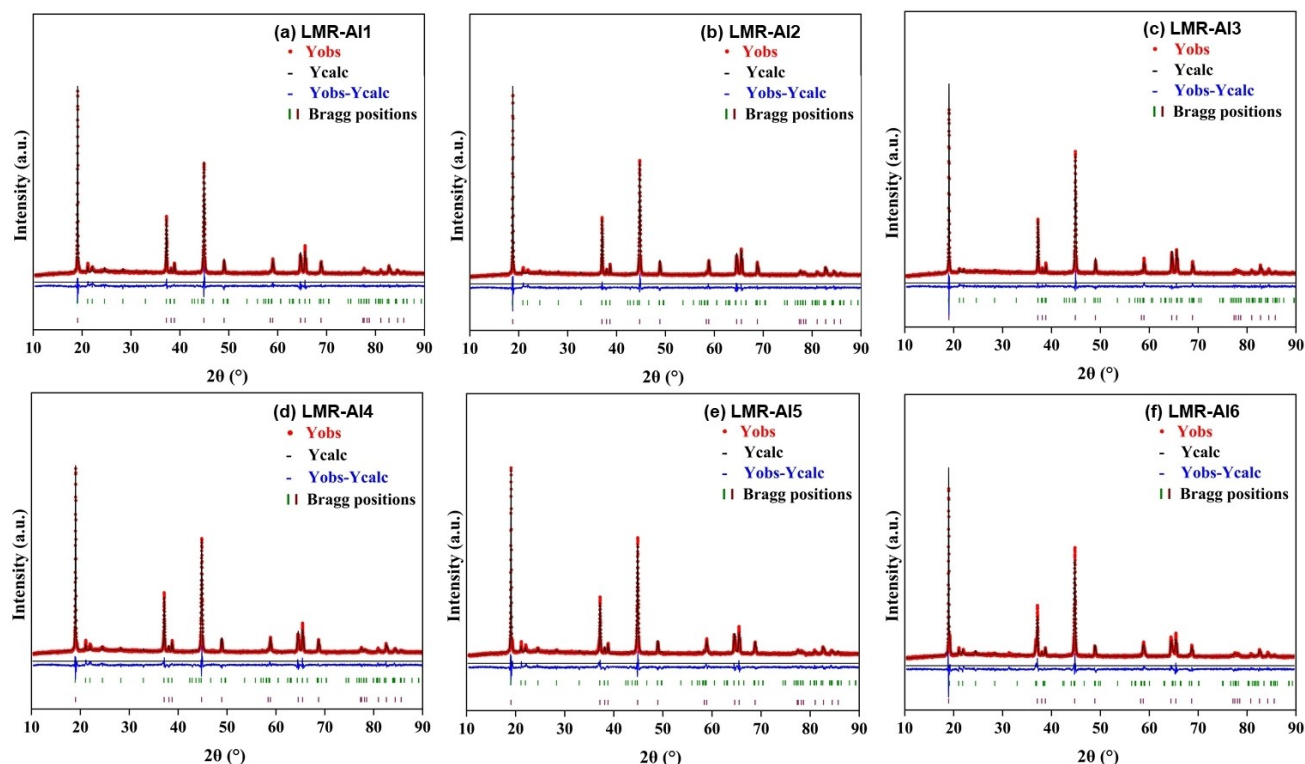
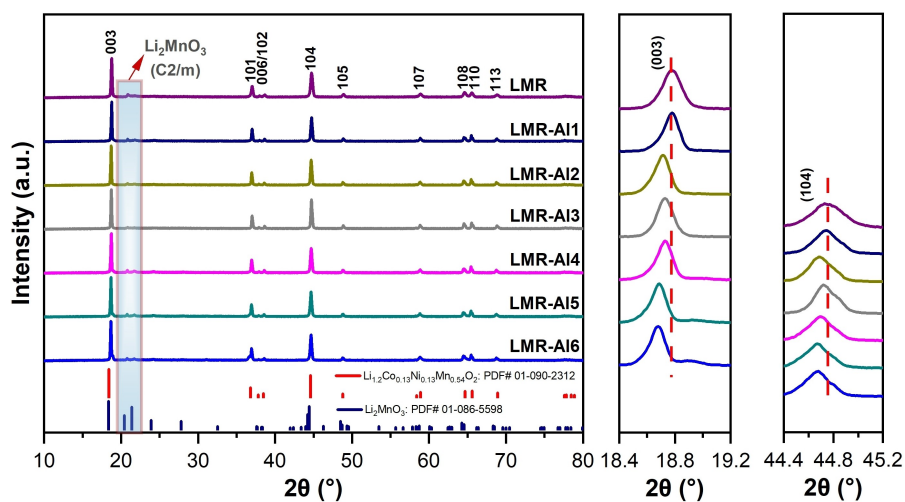**Figure 2.** Rietveld refinement results for LMRO cathode materials.

Figure 3. XRD patterns of LMRO cathode powders.

| Table 3. Rietveld refinement parameters of the LMRO cathode materials.							
Sample	a (Å)	c(Å)	c/a	R_{wp} (%)	R_b (%)	GOF	I(003)/I(104)
LMR	2.8506	14.1978	4.9807	5.55	4.29	1.01	1.80
LMR–Al1	2.8498	14.2308	4.9935	6.02	4.54	1.12	1.61
LMR–Al2	2.8480	14.2277	4.9957	5.92	4.44	1.10	1.56
LMR–Al3	2.8472	14.2379	5.0007	5.40	4.17	0.98	1.50
LMR–Al4	2.8495	14.2217	4.9910	6.35	4.76	1.18	1.58
LMR–Al5	2.8472	14.2138	4.9921	6.39	4.77	1.18	1.54
LMR–Al6	2.8490	14.2472	5.0008	6.58	4.85	1.34	1.53

Mn sites, modifying the local atomic arrangement and strengthening the layered framework

In nickel-containing layered cathodes, Li/Ni mixing is a well-known issue that negatively impacts electrochemical performance. The ionic radii of Li^+ (0.76 Å) and Ni^{2+} (0.69 Å) are very similar, leading to cation disorder where Ni^{2+} partially replaces Li^+ in the Li-layer. This effect can block lithium diffusion pathways, resulting in higher polarization, lower initial discharge capacity, and poor long-term cycling stability.[40] How-ever, the c/a ratio (>4.9) and I(003)/I(104) intensity ratio (>1.2) observed in Table 3 confirm that Al-doped LMRO materials exhibit a well-ordered layered structure with minimal Li/Ni mixing. These structural attributes contribute to the enhanced electrochemical performance observed in Al-doped samples.

The EIS results of LMRO cathodes before and after cycling are presented in Figure 4, and the fitted R_s and R_{ct} values are listed in Table 4. The equivalent circuit model includes R_s, representing the electrolyte resistance, R_{ct}, which corresponds
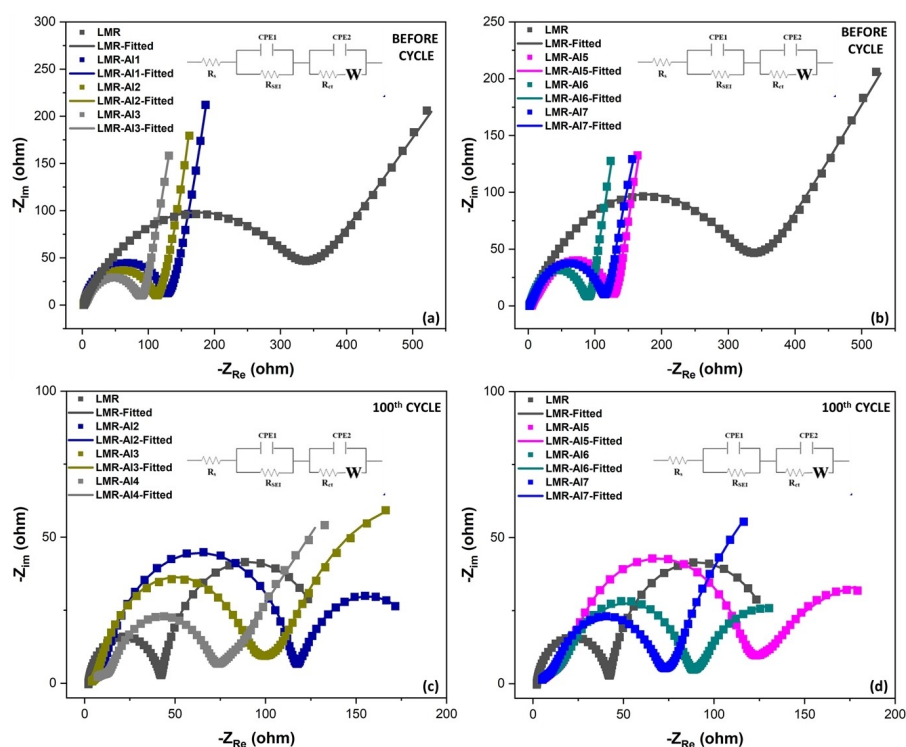
Figure 4. EIS spectra of LMRO cathode materials before cycling (a) LMR, LMR–Al1, LMR–Al2, LMR–Al3, (b) LMR, LMR–Al4, LMR–Al5, LMR–Al6. EIS spectra of LMRO cathode materials after 100 cycle (c) LMR, LMR–Al1, LMR–Al2, LMR–Al3, (c) LMR, LMR–Al4, LMR–Al5, LMR–Al6 The inset shows the fitted equivalent circuit model.

Table 4.	EIS fitting data for LMRO cathode materials.					
	Cycle	R_s	R_{ct}	σ_w	D_{Li}	i_0
LMR	1st	2.092	315.4	61.5	3.02×10^{-18}	7.94×10^{-5}
	100th	2.130	92.79	33.4	9.18×10^{-18}	2.77×10^{-4}
LMR-Al1	1st	1.830	126.1	18.8	3.22×10^{-17}	2.04E-04
	100th	3.031	104.4	22.2	2.30×10^{-17}	2.46×10^{-4}
LMR-Al2	1st	1.775	110.5	17.3	3.41×10^{-17}	2.32×10^{-4}
	100th	2.439	128.9	24.6	1.88×10^{-17}	1.99×10^{-4}
LMR-Al3	1st	2.980	89.1	15.3	4.35×10^{-17}	2.88×10^{-4}
	100th	3.734	55.2	19.3	3.04×10^{-17}	4.64×10^{-4}
LMR-Al4	1st	6.957	122.8	12.6	6.35×10^{-17}	2.09×10^{-4}
	100th	4.198	96.3	19.6	2.95×10^{-17}	2.66×10^{-4}
LMR-Al5	1st	1.996	89.9	11.7	7.41×10^{-17}	2.85×10^{-4}
	100th	4.555	91.4	15.7	4.61×10^{-17}	2.81×10^{-4}
LMR-Al6	1st	2.780	116.2	15.1	4.45×10^{-17}	2.21×10^{-4}
	100th	4.827	65.4	16.0	4.46×10^{-17}	3.92×10^{-4}

to charge transfer resistance at high frequencies, and W, the Warburg impedance related to lithium-ion diffusion in the bulk material. Before cycling, LMR−Al5 exhibits the lowest R_{ct} (89.1 Ω), suggesting the most efficient initial charge transfer kinetics, while the pristine LMR cathode shows the highest R_{ct} (315.4 Ω), confirming that Al doping significantly reduces interfacial resistance. However, after 100 cycles, LMR−Al3 and LMR−Al6 show the lowest R_{ct} values (55.2 Ω and 65.4 Ω, respectively), suggesting that they maintain superior charge transfer over extended cycling. The lithium-ion diffusion coefficient, calculated from EIS, supports these findings. Before cycling, LMR−Al2 has one of the highest diffusion coefficient values (3.41×10^{-17} cm^2/s), indicating excellent lithium-ion transport properties. After 100 cycles, LMR−Al6 retains the highest diffusion coefficient (4.46×10^{-17} cm^2/s), followed by LMR−Al3 (3.04×10^{-17} cm^2/s). Despite this, LMR−Al2 still demonstrates the best overall electrochemical performance, suggesting that an optimal balance of charge transfer resistance, lithium diffusion, and structural stability is more critical than absolute values of R_{ct} or the diffusion coefficient alone. Similarly, Warburg impedance values indicate that LMR−Al2 has one of the lowest Warburg impedance values before cycling, confirming its superior initial lithium-ion transport. Although LMR−Al3 retains the most stable Warburg impedance after 100 cycles, the overall electrochemical performance trends suggest that LMR−Al2 maintains better capacity retention and rate capability despite its slightly higher post-cycling R_{ct} and diffusion coefficient. The exchange current density, which reflects charge transfer ability, follows a similar trend. Before cycling, LMR−Al3 and LMR−Al5 exhibit the highest exchange current density, while after 100 cycles, LMR−Al3 retains the highest exchange current density. However, the overall superior electrochemical performance of LMR−Al2 suggests that an optimal combination of charge transfer kinetics and lithium diffusion, rather than the absolute lowest R_{ct} or highest diffusion coefficient, is responsible for its enhanced cycling stability and rate performance. These findings indicate that while LMR−Al3 and LMR−Al6 exhibit the lowest R_{ct} and highest diffusion coefficient values after 100 cycles, their overall electrochemical performance is still slightly inferior to that of LMR−Al2, which demonstrates a more balanced optimization of charge transfer, diffusion properties, and structural integrity. This suggests that moderate Al doping, as in LMR−Al2, provides the best compromise between transport properties and capacity retention, leading to superior long-term electrochemical performance.

XPS results, given in Figure S3 (Supporting Information), confirm the site-specific substitution of Al in Li-rich Mn-based oxides and its effect on the oxidation states of transition metals. The presence of Al 2p peaks in LMR−Al1 and LMR−Al4, absent in pristine LMR, indicates successful Al incorporation. Mn 2p spectra of LMR−Al1 exhibit a shift in the Mn^{3+}/Mn^{4+} ratio, suggesting Al substitution at the Mn-site, which stabilizes Mn and mitigates oxygen loss. In contrast, Li 1s and O 1s spectra of LMR−Al4 suggest Al incorporation into the Li-site, influencing the local coordination environment without significantly altering Mn oxidation states. Ni 2p spectra remain largely unchanged across all samples, confirming that Al primarily

interacts with Mn rather than Ni. These findings indicate that Mn-site Al doping enhances structural stability, while Li-site Al doping contributes to improved Li-ion coordination.

The voltage plateau in Li-rich cathode materials ($(1-x)$LiMO$_2 \cdot x$Li$_2$MnO$_3$) is a unique feature that represents the release of oxygen and the extraction of lithium ions from the Li$_2$MnO$_3$ phase. This process is induced by complex chemical reactions and structural evolution. The reinsertion of lithium ions is associated with the reduction of transition metal species. The reversible insertion and extraction of lithium ions in subsequent cycles exhibit reduced voltage hysteresis, with no evidence of the voltage plateau at 4.5 V.[12,22] As shown in Figure 5, during the first charge cycle, a prominent voltage plateau is observed, corresponding to the activation of the Li$_2$MnO$_3$ phase, a process associated with oxygen loss. In the first cycle, a charge capacity exceeding 300 mAhg^{-1} was obtained, depending on the dopant level, while a high irreversible capacity loss was observed during the first discharge due to the relatively weak reversibility of this reaction. The Al-doping process contributed to the reduction of irreversible capacity loss, as confirmed by the first and second cycle coulombic efficiency (CE). The first cycle CE values for LMR−Al1, LMR−Al2, and LMR−Al3 were 64.61%, 56.20%, and 56.59%, respectively, while in the second cycle, the CE significantly improved to 100.89%, 99.89%, and 96.78%, indicating enhanced reaction reversibility. After the activation of Li$_2$MnO$_3$, there is a substantial improvement in CE, suggesting that Al
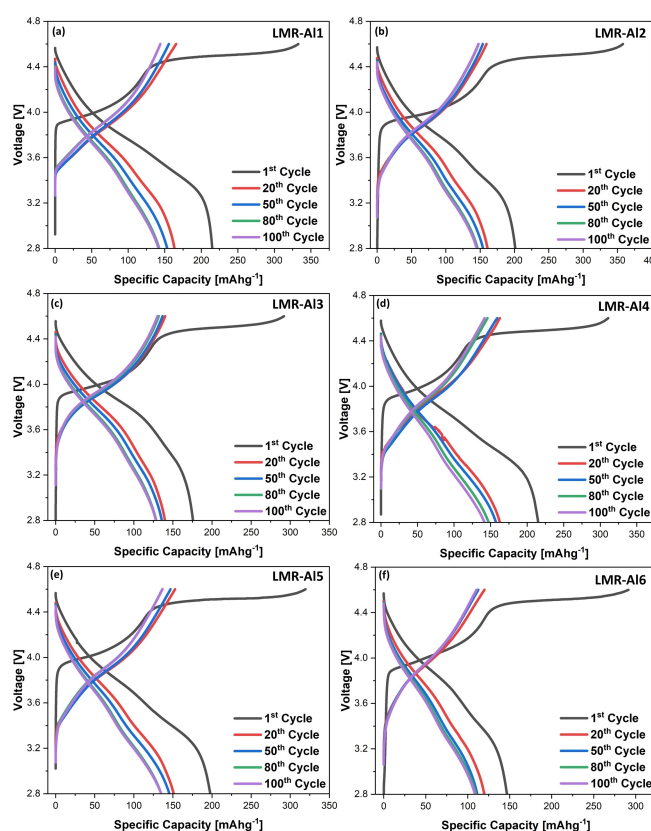
Figure 5. The charge/discharge profile (a) LMR−Al1, (b) LMR−Al2, (c) LMR−Al3, (d) LMR−Al4, (e) LMR−Al5, (f) LMR−Al6.

incorporation enhances structural stability and lithium-ion reversibility. The voltage profiles of LMRO cathodes over 100 cycles at 0.25 C within the potential window of 2.8–4.6 V are given in Figure 5(a)–(f), showing the 1st, 20th, 50th, 80th, and 100th cycles for each composition. Figure 5(a) shows the charge-discharge behavior of LMR–Al1, which demonstrates a relatively stable voltage profile but suffers from noticeable capacity fading. Figure 5(b) presents LMR–Al2 (0.02% Al doping at the Mn-site), which exhibits the best electrochemical performance, with higher first-cycle capacity, improved CE, and better retention over 100 cycles. Figure 5(c) illustrates the performance of LMR–Al3, where an increase in Al content results in greater voltage fade and lower long-term capacity retention compared to LMR–Al2. Figure 5(d), 5(e), and 5(f) show the charge-discharge behavior of Li-site Al-doped samples (LMR–Al4, LMR–Al5, and LMR–Al6, respectively), where increasing Al substitution leads to reduced initial capacities and accelerated performance degradation. As illustrated in Figure 5, the first specific charge capacities of LMR–Al1, LMR–Al2, and LMR–Al3 were 332.8, 357.9, and 310.4 mAhg^{-1}, respectively, demonstrating the beneficial effect of Al doping. The corresponding first specific discharge capacities were 215.1, 201.2, and 175.6 mAhg^{-1}, indicating a notable irreversible capacity loss in the first cycle. Among these compositions, LMR–Al2 (0.02% Al on Mn-site) exhibits the best overall electrochemical performance. This is evident in the first discharge capacity of 201.2 mAhg^{-1}, which is higher than that of LMR–Al1 (215.1 mAhg^{-1}) and LMR–Al3 (175.6 mAhg^{-1}). Furthermore, with increasing Al content, electrochemical performance deteriorates, as seen in LMR–Al3, which has a lower first discharge capacity and more pronounced capacity fading over 100 cycles. For the Li-site Al-doped cathodes, the first specific charge capacities of LMR–Al4, LMR–Al5, and LMR–Al6 were 342.5, 319.5, and 291.3 mAhg^{-1}, respectively, while the first discharge capacities were 222.5, 199.6, and 159.4 mAhg^{-1}, as shown in Figure 5(d)–(f). The CE in the first cycle were 64.96%, 61.88%, and 50.38%, respectively. However, in the second cycle, CE values improved significantly to 100.40%, 100.60%, and 93.70%, confirming the reduction of irreversible capacity loss after the first cycle. As shown in the long-term cycling data, LMR–Al2 exhibits the best cycle stability among all samples, retaining the highest discharge capacity after 100 cycles, confirming that 0.02% Al doping at the Mn-site provides the optimal balance between initial capacity, lithium diffusion kinetics, and long-term structural stability. In contrast, higher Al doping levels (LMR–Al3 and beyond) show faster capacity fading, further proving that excessive Al substitution negatively impacts electrochemical stability. The voltage profile of the LMR cathode is given in Figure S4 (supporting information). Previous studies have demonstrated that Al substitution in the Li layer decreases the band gap of Li_2MnO_3, increasing electronic conductivity and enhancing rate capability in LMRO cathode materials [19,23,27,30,46-48]. However, in this study, excessive Al doping leads to a progressive decline in electrochemical performance, confirming that 0.02% Mn-site Al doping is the optimal level for achieving the best electrochemical performance. These results conclusively prove that LMR–Al2 (0.02% Al

on Mn-site) demonstrates the best electrochemical performance, as evidenced by its higher first discharge capacity, improved Coulombic efficiency, and superior long-term cycling stability. Increasing the Al dopant level negatively affects the electrochemical performance, leading to reduced lithium-ion mobility, greater charge transfer resistance, and lower cycle retention over extended cycling.

In In a study by Zhao et al.,[49] an Al-doped Li-rich cathode exhibited an initial discharge capacity of approximately 250 mAhg^{-1}, with improved capacity retention over 100 cycles.

Yalcin et. al.[50] showed that Al doping in $Li_{1.20}Mn_{0.52-x}$-$Al_xNi_{0.20}Co_{0.08}O_2$ using a supercritical-CO_2-assisted method improved cycling stability, achieving ~250 mAhg^{-1} at 0.1 C with ~85% capacity retention after 100 cycles. In contrast, this study demonstrates that 0.02 at. % Mn-site Al doping provides the best performance, delivering ~238 mAhg^{-1} at 0.25 C with better long-term stability than higher doping levels. Overall, our findings support previous reports that moderate Al incorporation can effectively improve Li-rich cathode performance, while also demonstrating that maintaining an optimal doping concentration is crucial to prevent structural and electrochemical instability.

The cycle performance of pristine and Al-doped LMRO cathodes over 100 cycles is presented in Figure 6(a), while the corresponding Coulombic efficiencies are shown in Figure 6(b). The pristine LMR cathode exhibits the lowest capacity retention, confirming that Al doping significantly improves the cycling stability of Li-rich cathodes. Among the doped samples, LMR–Al2 maintains the highest specific discharge capacity after 100 cycles, demonstrating that 0.02% Al substitution at the Mn-
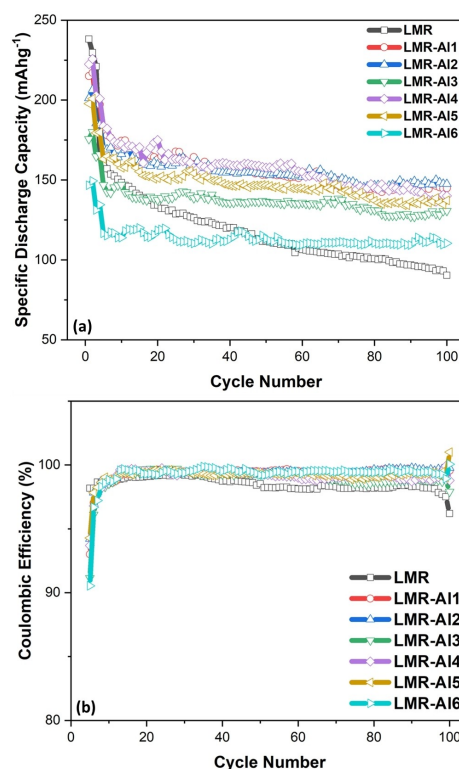

Figure 6. Cycling performance of LMRO cathodes at 2.8-4.6 V in 100 cycles.

site provides the best electrochemical performance. LMR–Al1 and LMR–Al3 show intermediate performance, with LMR–Al1 exhibiting slightly better capacity retention than LMR–Al3. However, both display a higher capacity fading rate compared to LMR–Al2, reinforcing that increasing Al content beyond 0.02% negatively affects long-term stability. The Li-site Al-substituted cathodes, including LMR–Al4, LMR–Al5, and LMR–Al6, show more pronounced capacity fading, with LMR–Al6 exhibiting the most rapid decline in performance. This suggests that Al substitution at the Mn-site is more effective in stabilizing electrochemical performance than Li-site substitution.

The Coulombic efficiency for all samples stabilizes above 99% after the initial activation cycles, indicating good reversibility. LMR–Al2 maintains consistently high Coulombic efficiency throughout cycling, further confirming its superior electrochemical stability. LMR–Al6 shows slightly lower Coulombic efficiency fluctuations, which could be attributed to increased interfacial resistance or side reactions. The pristine LMR cathode also maintains stable Coulombic efficiency, but its significantly lower capacity compared to the doped samples suggests that while its cycling reversibility remains intact, its practical energy density is greatly reduced. Initial charge/discharge capacity and the coulombic efficiency of the LMRO cathodes are given in Table S1 (supporting information).

These results confirm that LMR–Al2, with 0.02% Al substitution at the Mn-site, exhibits the best electrochemical performance in terms of both capacity retention and Coulombic efficiency stability over 100 cycles. Increasing the Al substitution level leads to performance deterioration, with higher concentrations contributing to faster capacity fading. Mn-site substitution is more beneficial than Li-site substitution, as demonstrated by the superior performance of LMR–Al2 compared to the Li-substituted samples. Coulombic efficiency remains high for all compositions after the initial cycles, suggesting that Al substitution does not introduce severe side reactions but still affects capacity retention depending on the doping site and level. These findings confirm that 0.02% Al substitution at the Mn-site provides the optimal balance of capacity, cycling stability, and electrochemical efficiency, while excessive Al substitution compromises long-term performance.

To better understand between phase transition and voltage decay and to observe dopant effect on the materials, Figure 7 shows the differential capacity vs. voltage (dQ/dV) curves for 1st, 20th, 50th, 80th, and 100th cycle. dQ/dV curves for pristine LMR cathode is given in Figure S5 (Supporting Information)
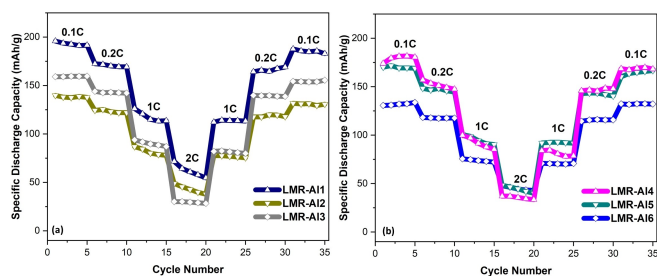
The first peak (~3.85–3.95 V) in the initial cycles is primarily associated with the oxidation of Ni^{2+} to Ni^{3+} and Co^{3+} to Co^{4+}, while the second peak (~4.05–4.15 V) corresponds to the continued oxidation of Ni^{3+} to Ni^{4+}, which may also involve anionic redox contributions from oxygen. These redox processes play a critical role in the charge compensation mechanism of Li-rich cathodes. During the first cycle, dQ/dV curves reveal two distinct oxidation peaks around 4.0 V for LMR–Al3 and LMR–Al6. The first peak (~3.9 V) is attributed to the oxidation of Ni^{2+} to Ni^{3+}, while the second peak (~4.1 V) corresponds to the oxidation of Co^{3+} to Co^{4+}. The presence of these two peaks in
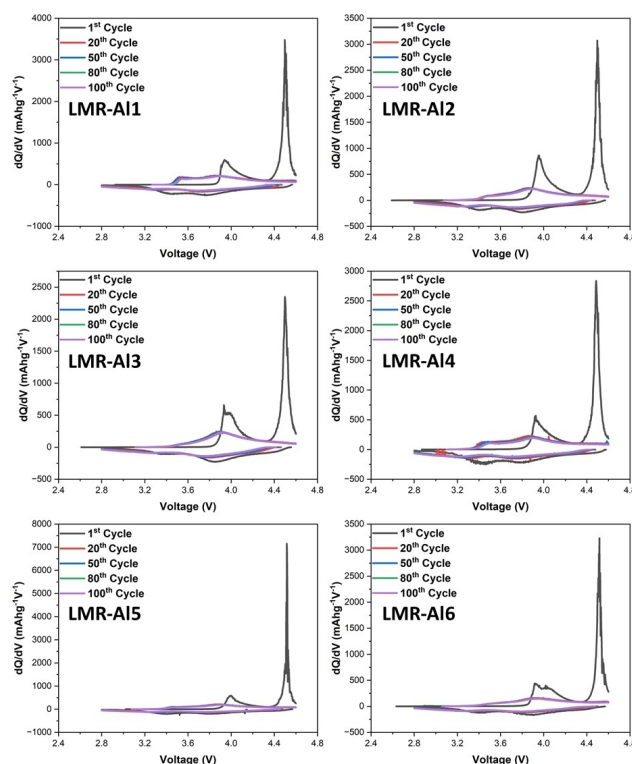
Figure 7. The dQ/dV curves (a) LMR–Al1, (b) LMR–Al2, (c) LMR–Al3, (d) LMR–Al4, (e) LMR–Al5, (f) LMR–Al6.

LMR–Al3 and LMR–Al6, but not in other samples, suggests a correlation between peak splitting and the dopant concentration. These two samples contain the highest Al substitution levels, which may influence the local electronic structure and coordination environment of the transition metal ions, resulting in more distinct redox processes.

Over extended cycling, these oxidation peaks gradually merge into a broader single peak, likely due to structural rearrangements and increased electronic delocalization. The observed peak merging could be attributed to the progressive redistribution of transition metal ions and increased cation disorder, leading to changes in the electronic environment and a reduction in the separation between Ni and Co redox processes. In the charge process, a subsequent peak near 4.5 V is associated with the activation of the Li_2MnO_3 phase, which involves oxygen redox activity. This activation process is often accompanied by oxygen release and structural reorganization, contributing to the initial capacity loss observed in Li-rich cathodes. The degree of voltage fade differs depending on the dopant site and level. In the LMR sample, oxidation and reduction peaks shift significantly downward (~100–150 mV over 100 cycles), confirming severe voltage decay. In contrast, Mn-site Al-doped samples exhibit improved voltage retention, with peak shifts limited to ~50 mV over 100 cycles, indicating better structural stability. However, Li-site Al-doped samples experience more substantial peak shifts (~120 mV over 100 cycles), suggesting higher resistance and reduced long-term stability. In samples with lower Al doping levels, such as

Figure 8. Rate capability of the LMRO cathodes in the voltage range of 2.8–4.6 V at various C-rate.

rich cathode materials. The XRD patterns show that the structure of Al-doped LMRO cathode materials is well-organized. The substitution of Al into the lattice does not lead to any impurities or change the crystalline structure. The C-rate test results show that 0.02 at. % Al dopant on Li- and Mn-site significantly improves the rate performance of Li-rich cathode materials, reducing structural degradation during charge/discharge cycles. Al doping enhances structural stability, allowing for higher initial discharge capacities. Al doping reduced irreversible capacity loss in the first cycle and improved the second coulombic efficiency. The experimental results demonstrate that the material performance is significantly improved.

LMR–Al1 and LMR–Al4, the redox peaks remain distinct, and the voltage fade is moderate, demonstrating a more stable electrochemical environment. The presence of two distinct oxidation peaks in LMR–Al3 and LMR–Al6, along with their more significant peak evolution over cycling, suggests that higher Al doping levels alter the electrochemical reaction pathways. This may be due to modifications in the local electronic environment, which affect the redox activity of Ni and Co and lead to increased polarization. The differences in redox peak behavior further confirm that excessive Al doping, particularly at high levels in both Mn- and Li-sites, introduces structural and kinetic complexities that accelerate voltage decay and impact long-term electrochemical performance. Figure 8 shows the C-rate test results of Al-doped LMRO cathodes. The material's rate performance has been significantly improved with a 0.02 Al dopant.

However, as the dopant level increases, the rate performance proportionally decreases. The Al doping process has enhanced the structural stability of Li-rich cathode materials. The substitution of Al into the crystal lattice can be affected to reduce of the structural degradation during charge/discharge cycles. This improved stability particularly aids in maintaining capacity at high C-rates. Al-doped Li-rich cathodes generally exhibit higher initial discharge capacities. This improvement can be attributed to the enhanced electronic conductivity and better structural integrity provided by Al doping. The observed enhancement in capacity and rate performance of the Al-doped LMROs suggests that Al doping may address issues such as electrolyte decomposition and transition metal dissolution, which deteriorate battery performance over time. However, as the dopant level increased, lattice distortions and structural stress may have increased. This distortion can block the diffusion pathways of lithium ions, slowing down kinetics and leading to a decrease in capacity.

Conclusions

In summary, Al-doped lithium-rich layered oxides $Li_{1.2}Mn_{0.54-x}Ni_{0.13}Co_{0.13}Al_xO_2$ and $Li_{1.2-x}Mn_{0.54}Ni_{0.13}Co_{0.13}Al_xO_2$ (x = 0.02, 0.05, 0.1) were successfully synthesized by a sol-gel method based on elemental analysis results by ICP-MS, and their electrochemical performances were compared. XRD analysis revealed that all the samples have the layered phase, characteristic of Li-

Conflict of Interests

The authors declare no conflict of interest.

Data Availability Statement

The data that support the findings of this study are available from the corresponding author upon reasonable request.

Keywords: Li-rich oxides · Al-doping · Li-ion batteries · Cathode materials

[1] J. B. Goodenough, K. S. Park, *J. Am. Chem. Soc.* **2013**, *135*(4), 1167–1176.
[2] V. Etacheri, R. Marom, R. Elazari, G. Salitra, D. Aurbach, *Energy Environ. Sci.* **2011**, *4*(9), 3243–3262.
[3] D. Deng, *Energy Sci. Eng.* **2015**, *3*, 385–418.
[4] H. Li, Z. Wang, L. Chen, X. Huang, *Adv. Mater.* **2009**, *21*(45), 4593–4607.
[5] N. Nitta, F. Wu, J. T. Lee, G. Yushin, *Mater. Today* **2015**, *18*(5), 252–264.
[6] M. H. Rossouw, M. M. Thackeray, *Mater. Res. Bull.* **1991**, *26*(6), 463–473.
[7] M. M. Thackeray, S. H. Kang, C. S. Johnson, J. T. Vaughey, S. A. Hackney, *Electrochem. Commun.* **2006**, *8*(9), 1531–1538.
[8] M. M. Thackeray, S. H. Kang, C. S. Johnson, J. T. Vaughey, S. A. Hackney, *J. Mater. Chem.* **2007**, *17*(30), 3112–3125.
[9] M. Akhilash, P. S. Salini, B. John, T. D. Mercy, *J. Alloys Compd.* **2021**, *869*, 159239.
[10] W. Zuo, M. Luo, X. Liu, J. Wu, H. Liu, J. Li, Y. Yang, *Energy Environ. Sci.* **2020**, *13*(12), 4450–4497.
[11] Y. Fan, W. Zhang, Y. Zhao, Z. Guo, Q. Cai, *Energy Storage Mater.* **2021**, *40*, 51–71.
[12] W. He, W. Guo, H. Wu, L. Lin, Q. Liu, X. Han, D. L. Peng, *Adv. Mater.* **2021**, *33*(50), 2005937.
[13] D. Shumei, T. Dan, L. Ping, L. Huiqin, W. Fenyan, H. Zhang, *J. Solid State Electrochem.* **2023**, *27*(1), 1–23.
[14] P. K. Nayak, J. Grinblat, E. Levi, M. Levi, B. Markovsky, D. Aurbach, *Phys. Chem. Chem. Phys.* **2017**, *19*(8), 6142–6152.
[15] C. C. Wang, Y. C. Lin, K. F. Chiu, *J. Alloys Compd.* **2017**, *721*, 600–608.
[16] A. Choi, J. Lim, H. J. Kim, S. C. Jung, H. W. Lim, H. Kim, K. T. Lee, *Adv. Energy Mater.* **2018**, *8*(11), 1702514.
[17] P. Oh, J. Yun, S. Park, G. Nam, M. Liu, J. Cho, *Adv. Energy Mater.* **2021**, *11*(15), 2003197.
[18] L. Nie, S. Chen, W. Liu, *Nano Res.* **2023**, *16*(1), 391–402.
[19] M. Iftekhar, N. E. Drewett, A. R. Armstrong, D. Hesp, F. Braga, S. Ahmed, L. J. Hardwick, *J. Electrochem. Soc.* **2014**, *161*(14), A2109.
[20] E. Zhao, Z. Hu, L. Xie, X. Chen, X. Xiao, X. Liu, *RSC Adv.* **2015**, *5*(39), 31238–31244.
[21] S. Li, L. Yang, Z. Liu, C. Zhang, X. Shen, Y. Gao, L. Chen, *Energy Storage Mater.* **2023**, *55*, 356–363.
[22] S. Zhao, K. Yan, J. Zhang, B. Sun, G. Wang, *Angew. Chem. Int. Ed.* **2021**, *60*(5), 2208–2220.

Batteries & Supercaps

Research Article
doi.org/10.1002/batt.202400652

Chemistry Europe
European Chemical
Societies Publishing

[23] X. Cai, N. Zhang, H. Ding, D. Zhao, J. Zhou, J. Zhang, S. Li, *Acta Mater.* **2023**, *258*, 119220.

[24] S. Zhao, Z. Guo, K. Yan, S. Wan, F. He, B. Sun, G. Wang, *Energy Storage Mater.* **2021**, *34*, 716–734.

[25] P. Liu, H. Zhang, W. He, T. Xiong, Y. Cheng, Q. Xie, D. L. Peng, *J. Am. Chem. Soc.* **2019**, *141*(27), 10876–10882.

[26] S. J. Cho, M. J. Uddin, P. K. Alaboina, S. S. Han, M. I. Nandasiri, Y. S. Choi, D. Choi, *Advanced Sustainable Systems* **2017**, *1*(7), 1700026.

[27] C. Song, W. Feng, X. Wang, Z. Shi, *J. Electroanal. Chem.* **2020**, *862*, 113962.

[28] W. Yu, L. Zhao, Y. Wang, H. Huang, S. Zhang, H. Li, A. Li, *J. Alloys Compd.* **2023**, *947*, 169481.

[29] A. Celeste, F. Girardi, L. Gigli, V. Pellegrini, L. Silvestri, S. Brutti, *Electrochim. Acta* **2022**, *428*, 140737.

[30] H. Guo, Y. Xia, H. Zhao, C. Yin, K. Jia, F. Zhao, Z. Liu, *Ceram. Int.* **2017**, *43*(16), 13845–13852.

[31] A. Celeste, R. Brescia, G. Greco, P. Torelli, S. Mauri, L. Silvestri, S. Brutti, *ACS Appl. Energ. Mater.* **2022**, *5*(2), 1905–1913.

[32] D. De Sloovere, S. K. Mylavarapu, J. D'Haen, T. Thersleff, A. Jaworski, J. Grins, A. Hardy, *Small* **2024**, 2400876.

[33] A. Celeste, M. Tuccillo, A. S. Menon, W. Brant, D. Brandell, V. Pellegrini, S. Brutti, *Small Methods* **2024**, 2301466.

[34] H. Yan, Y. H. Luo, Y. Lei, Q. L Pan, J. C. Zheng, *J. Alloys Compd.* **2024**, *993*, 174564.

[35] H. X. Wei, H. X, Y. M. Liu, Y. H. Luo, Y. D. Huang, L. B. Tang, Z. Y. Wang, J. C. Zheng, *Adv. Funct. Mater.* **2024**, *34*(7), 2307583.

[36] H. X. Wei, Y. H. Luo, Z. Y. Wang, H. Z. Chen, L. B. Tang, X. H. Zhang, J. C. Zheng, *Electrochim. Acta* **2024**, *475*, 143665.

[37] S. Zhang, Y. Ye, Z. Chen, Q. Lai, T. Liu, Q. Wang, S. Yuan, *Materials* **2023**, *16*(16), 5655.

[38] Y. Liang, S. Li, J. Xie, L. Yang, W. Li, C. Li, X. Shangguan, *New J. Chem.* **2019**, *43*(30), 12004–12012.

[39] W. Jiang, C. Zhang, Y. Feng, B. Wei, L. Chen, R. Zhang, W. Wei, *Energy Storage Mater.* **2020**, *32*, 37–45.

[40] Z. Huang, X. Li, Y. Liang, Z. He, H. Chen, Z. Wang, H. Guo, *Solid State Ionics* **2015**, *282*, 88–94.

[41] Y. Xu, M. Zhang, L. Yi, K. Liang, *J. Alloys Compd.* **2021**, *865*, 158899.

[42] Z. Huang, X. Wang, W. Feng, W. Li, Z. Shi, Z. Lei, *J. Electroanal. Chem.* **2021**, *895*, 115439.

[43] Z. Tai, X. Li, W. Zhu, M. Shi, Y. Xin, S. Guo, Y. Liu, *J. Colloid Interface Sci.* **2020**, *570*, 264–272.

[44] Z. Chen, J. Meng, Y. Wang, Q. Ma, F. Lai, Z. Li, S. Zhong, *Electrochim. Acta* **2021**, *378*, 138138.

[45] X. Jin, Q. Xu, H. Liu, X. Yuan, Y. Xia, *Electrochim. Acta* **2014**, *136*, 19–26.

[46] P. K. Nayak, J. Grinblat, M. Levi, E. Levi, S. Kim, J. W. Choi, D. Aurbach, *Adv. Energy Mater.* **2017**, *6*(8), 1502398.

[47] W. Yan, Y. Xie, J. Jiang, D. Sun, X. Ma, Z. Lan, Y. Jin, *ACS Sustainable Chem. Eng.* **2018**, *6*(4), 4625–4632.

[48] E. Zhao, X. Yu, F. Wang, H. Li, *Science China Chemistry* **2017**, *60*, 1483–1493.

[49] X. Zhao, M. Yang, J. Wang, D. Wang, *Chem. Res. Chin. Univ.* **2023**, *39*(4), 630–635.

[50] A. Yalçın, M. O. Güler, M. Demir, M. Gönen, M. Akgün, *ACS Omega* **2024**, *9*(47), 46813–46821.